Pressure-induced superconductivity in kagome metal CsCr3Sb5: Role of spin-orbit coupling and inter-orbital spin fluctuations

Wei Wang(王巍), Shun-Li Yu(于顺利), and Jian-Xin Li(李建新)
Citation: Chin. Phys. B, 2026, 35 (**2**): 027401. DOI: 10.1088/1674-1056/ae23ae
http://cpb.iphy.ac.cn; http://iopscience.iop.org/cpb

What follows is a list of articles you may be interested in

Pressure-stabilized Li2K electride with superconducting behavior

Xiao-Zhen Yan(颜小珍), Quan-Xian Wu(邬泉县), Lei-Lei Zhang(张雷雷), and Yang-Mei Chen(陈杨梅)
Chin. Phys. B, 2025, 34 (**9**): 097405. DOI: 10.1088/1674-1056/add009

Superconductivity and band topology of double-layer honeycomb structure M2N2 (M = Nb, Ta)

Jin-Han Tan(谭锦函), Na Jiao(焦娜), Meng-Meng Zheng(郑萌萌), Ping Zhang(张平), and Hong-Yan Lu(路洪艳)
Chin. Phys. B, 2025, 34 (**9**): 097402. DOI: 10.1088/1674-1056/adee04

Pairing correlation of the kagome-lattice Hubbard model with the nearest-neighbor interaction

Chen Yang(杨晨), Chao Chen(陈超), Runyu Ma(马润宇), Ying Liang(梁颖), and Tianxing Ma(马天星)
Chin. Phys. B, 2024, 33 (10): 107404. DOI: 10.1088/1674-1056/ad7578

Experimental observation of Fermi-level flat band in novel kagome metal CeNi5

Xue-Zhi Chen(陈学智), Le Wang(王乐), Shuai Zhang(张帅), Ren-Jie Zhang(张任杰), Yi-Wei Cheng(程以伟), Yu-Dong Hu(胡裕栋), Cheng-Nuo Meng(孟承诺), Zheng-Tai Liu(刘正太), Bai-Qing Lv(吕佰晴), and Yao-Bo Huang(黄耀波)
Chin. Phys. B, 2024, 33 (**8**): 087402. DOI: 10.1088/1674-1056/ad4019

Superconducting properties of the C15-type Laves phase ZrIr2 with an Ir-based kagome lattice

Qing-Song Yang(杨清松), Bin-Bin Ruan(阮彬彬), Meng-Hu Zhou(周孟虎), Ya-Dong Gu(谷亚东), Ming-Wei Ma(马明伟), Gen-Fu Chen(陈根富), and Zhi-An Ren(任治安)
Chin. Phys. B, 2023, 32 (**1**): 017402. DOI: 10.1088/1674-1056/aca3a2

RAPID COMMUNICATION

Pressure-induced superconductivity in kagome metal $CsCr_3Sb_5$: Role of spin–orbit coupling and inter-orbital spin fluctuations

Wei Wang(王巍)[1,2], Shun-Li Yu(于顺利)[3,4,†], and Jian-Xin Li(李建新)[3,4,‡]

[1] *School of Science, Nanjing University of Posts and Telecommunications, Nanjing* 210023, *China*
[2] *Jiangsu Physical Science Research Center, Nanjing* 210093, *China*
[3] *National Laboratory of Solid State Microstructures and Department of Physics, Nanjing University, Nanjing* 210093, *China*
[4] *Collaborative Innovation Center of Advanced Microstructures, Nanjing University, Nanjing* 210093, *China*

(Received 23 September 2025; revised manuscript received 22 November 2025; accepted manuscript online 25 November 2025)

Motivated by the recent discovery of superconductivity in the kagome metal $CsCr_3Sb_5$ under pressure, we theoretically investigate the superconducting pairing symmetry and the impact of spin–orbit coupling (SOC) in this system. By employing an effective four-orbital tight-binding model and solving the linearized gap equation within the random phase approximation, we find that the large inter-orbital spin fluctuations enhanced by Hund's coupling promote a superconducting gap function with E_{2g} symmetry. The inclusion of SOC further stabilizes this gap symmetry. Our analysis also reveals that the $d_{x^2-y^2}$ orbital plays the dominant role in forming the superconducting pairs.

Keywords: kagome lattice, $CsCr_3Sb_5$, superconductivity, spin–orbit coupling

PACS: 74.20.Rp, 75.10.Lp, 71.70.Ej, 71.10.Fd

DOI: 10.1088/1674-1056/ae23ae **CSTR:** 32038.14.CPB.ae23ae

1. Introduction

Kagome lattice, a network of corner-sharing triangles, has been extensively studied in condensed matter physics for its ability to realize unconventional magnetic and electronic states.[1–10] Recently, significant attention has been drawn to the newly discovered quasi-two-dimensional kagome metals AV_3Sb_5 (A = K, Rb, Cs) owing to their rich phenomena.[11–16] Reported properties include a giant anomalous Hall effect,[17] an unconventional charge density wave (CDW) phase accompanied by time-reversal symmetry breaking,[18] pair density wave,[19] electronic nematicity,[20] and superconductivity (SC).[20–24]

The newly synthesized kagome metal $CsCr_3Sb_5$ [Fig. 1(b)], a structural analogue of the AV_3Sb_5 family, exhibits a distinct phase diagram.[25] At ambient pressure, it undergoes a transition near 55 K that simultaneously involves CDW, spin density wave (SDW), and orbital nematicity.[25,26] Under applied pressure, these density-wave (DW) phases are progressively suppressed and coexist with SC around 3.65–3.80 GPa before being eliminated, giving rise to a superconducting dome that peaks at 4.2 GPa with a transition temperature of 6.4 K and vanishes above 10 GPa.[25] Moreover, the absence of a soft acoustic phonon mode suggests that the SC phase is unconventional.[27]

Unlike AV_3Sb_5, where the Fermi level resides near van Hove singularities,[16] $CsCr_3Sb_5$ hosts a flat band derived from the Cr d orbitals near the Fermi level and van Hove singularities with binding energy of ~ 0.5 eV, observed in both angle-resolved photoemission spectroscopy experiments[28–30] and theoretical calculations.[31–34] A random phase approximation (RPA) study[35] employing a 30-orbital tight-binding model for $CsCr_3Sb_5$ suggests an $s^{\pm}$-wave pairing instability with competing (d_{xy}, $d_{x^2-y^2}$)-wave symmetry. However, due to the significantly smaller differences in the on-site energies between d orbitals in $CsCr_3Sb_5$ compared to AV_3Sb_5[36] (see Appendix A), spin–orbit coupling (SOC) in $CsCr_3Sb_5$ may play a more prominent role than in AV_3Sb_5. Indeed, introducing a small SOC can lead to a qualitative change in the Fermi surface (FS) structure [see Figs. 1(c) and 1(d)]. Therefore, similar to some iron-based superconductors,[37–40] although the low-energy electronic structure is dominated by 3d electrons, SOC could have a significant impact on the superconducting pairing symmetry in $CsCr_3Sb_5$.

In this paper, using an effective four-orbital tight-binding model with local multi-orbital Hubbard interactions and an RPA analysis, we investigate the effect of SOC on the superconducting pairing symmetry in pressurized $CsCr_3Sb_5$. Our results reveal that the E_{2g} symmetry is the dominant pairing symmetry both with and without SOC, except in the regime of very small Hund's coupling without SOC, where the A_{2g} symmetry becomes stabilized. The enhancement of the inter-orbital spin fluctuations stabilizes the E_{2g} symmetry. When the

†Corresponding author. E-mail: slyu@nju.edu.cn
‡Corresponding author. E-mail: jxli@nju.edu.cn

SOC is included, spin fluctuations remain the primary driving force for pairing, with orbital fluctuations playing a subsidiary role. In both cases, the dominant pairing interaction originates from the β band, primarily derived from the $d_{x^2-y^2}$ orbital.

2. Model and method

To study the superconductivity of $CsCr_3Sb_5$, we first perform the first-principles calculation (see details in Appendix A) on $CsCr_3Sb_5$ under external pressure of 5 GPa. Structural relaxation yielded a hexagonal lattice [Fig. 1(b)] with parameters $a = 5.3235$ Å and $c = 8.6439$ Å. Figure 1(a) presents the resulting electronic band structure and projected density of states, revealing the dominant contributions near the Fermi energy from the Cr-d_{xz}, Cr-d_{yz}, Cr-$d_{x^2-y^2}$, and Sb_1-p_z orbitals. Furthermore, the bands originating from the Cr d orbitals exhibit minimal dispersion along the Γ–A path, resulting in the flat bands. To capture these features, we employed the effective four-orbital tight-binding model H_t established in our previous work,[34] which incorporates the Cr-d_{xz}, Cr-d_{yz}, Cr-$d_{x^2-y^2}$, and Sb_1-p_z orbitals, to fit the DFT-calculated bands in the $k_z = 0$ plane at 5 GPa. The hopping parameters for $CsCr_3Sb_5$ under pressure are given in Appendix A. As shown in Fig. 1(a), the effective tight-binding model qualitatively reproduces the bands in the DFT calculations near the Fermi level.

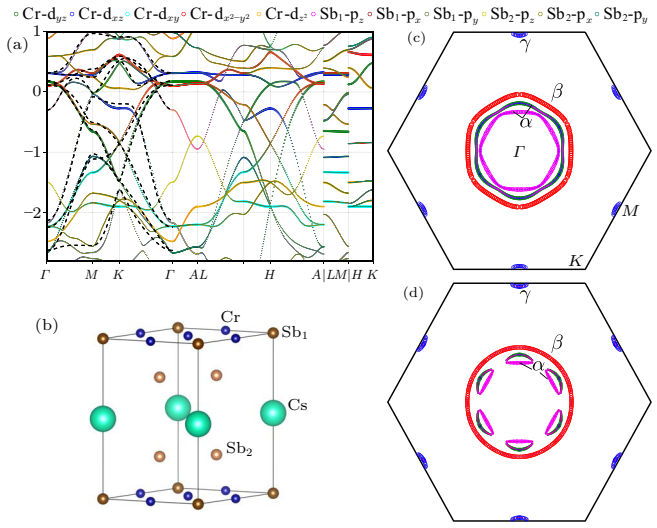

Fig. 1. (a) Electronic band structure and projected density of states of $CsCr_3Sb_5$ without SOC at 5 GPa. The Fermi level is set to zero. The dashed black lines denote the band structure derived from the effective tight-binding model. (b) Crystal structure of $CsCr_3Sb_5$. Orbital-resolved density of states projected onto the FS of $CsCr_3Sb_5$ (c) without SOC and (d) with SOC ($\lambda_{SOC} = 0.025$ eV), obtained from the effective tight-binding model. The color-coded circles in (a), (c), and (d) represent orbital contributions. The symbols α, β, and γ denote three distinct bands.

To investigate the influence of SOC on superconducting pairing function, we restrict the SOC to on-site terms, defined as $H_{SOC} = \lambda_{SOC}\sum_i \boldsymbol{l}_i \cdot \boldsymbol{s}_i$, where $\boldsymbol{s}_i$ and $\boldsymbol{l}_i$ denote the spin and orbital angular momentum operators, respectively, for the i-th Cr atom (see Appendix A). The total Hamiltonian is then expressed as $H = H_t + H_{SOC} + H_I$, where H_I corresponds to the local multi-orbital Hubbard-type interaction for Cr d-electrons (see Appendix B), parametrized by the Hubbard U, inter-orbital Coulomb interaction U' and Hund's coupling J_H. Based on the single-particle Hamiltonian $H_0 = H_t + H_{SOC}$, we present the orbital-resolved FSs in Figs. 1(c) and 1(d), calculated without and with SOC, respectively. In both cases, the bands denoted by α originate predominantly from the Sb_1-p_z and Cr-d_{yz} orbitals near the Fermi level, while the bands β and γ are primarily contributed by the Cr-$d_{x^2-y^2}$ and Cr-d_{xz} orbitals, respectively.

To explore the superconducting pairing symmetry in $CsCr_3Sb_5$ under pressure, we solve the linearized gap equation projected onto the FS, formulated as an eigenvalue problem:[40–43]

$$\lambda\Delta_\xi(\boldsymbol{k}_F) = \sum_{\xi'}\int_{FS'} M^{\xi\xi'}(\boldsymbol{k}_F,\boldsymbol{k}'_F)\Delta_{\xi'}(\boldsymbol{k}'_F). \tag{1}$$

The pairing kernel is given by

$$M^{\xi\xi'}(\boldsymbol{k}_F,\boldsymbol{k}'_F) = -\frac{1}{V_{BZ}}\frac{dk'}{|v_F(\boldsymbol{k}'_F)|}\Gamma^{\xi\xi'}(\boldsymbol{k}_F,\boldsymbol{k}'_F), \tag{2}$$

where $|v_F(\boldsymbol{k}'_F)|$ corresponds to the Fermi velocity at the Fermi momentum $\boldsymbol{k}'_F$, V_{BZ} denotes the volume (or area in two dimensions) of the Brillouin zone, and the indices ξ label the (pseudo)spin-singlet ($\xi = 0$) and triplet ($\xi = x,y,z$) pairing channels. $\Gamma^{\xi\xi'}(\boldsymbol{k}_F,\boldsymbol{k}'_F)$ represents the effective pairing interaction projected onto the FS (see Appendix B). The linearized gap equation (Eq. (1)) yields eigenvalues λ and eigenvectors $\Delta_\xi(\boldsymbol{k}_F)$, which correspond to the superconducting gap functions. A leading eigenvalue reaching $\lambda = 1$ indicates the onset of a superconducting instability, unless it is suppressed by a competing instability in the particle–hole channel. To examine the possibility of such particle–hole instabilities within the RPA framework, we diagonalize the matrix $-\hat{V}\hat{\chi}_0(\boldsymbol{q},0)$, where $\hat{\chi}_0(\boldsymbol{q},0)$ is the bare particle–hole susceptibility and $\hat{V}$ is the bare interaction vertex (see Appendix B). An eigenvalue of $-\hat{V}\hat{\chi}_0(\boldsymbol{q},0)$ attaining unity, corresponding to the Stoner criterion, signals the emergence of a particle–hole instability.

Since the spin-fluctuation-mediated pairing interaction $\Gamma^{\xi\xi'}(\boldsymbol{k}_F,\boldsymbol{k}'_F)$ is directly related to the particle–hole susceptibility $\hat{\chi}(\boldsymbol{q} = \boldsymbol{k}_F - \boldsymbol{k}'_F, 0)$ (see Appendix B), it is crucial to analyze which particle–hole fluctuations provide the dominant contribution. To this end, we diagonalize the static particle–hole susceptibility $\hat{\chi}(\boldsymbol{q},0)$ and consider the leading eigenvalues $\lambda_\chi^{max}(\boldsymbol{q})$. When the eigenvalue $\lambda_\chi^{max}(\boldsymbol{q})$ is strongly enhanced at a characteristic wave vector $\boldsymbol{Q}$, the scattering amplitude $\Gamma^{\xi\xi'}(\boldsymbol{k}_F,\boldsymbol{k}'_F)$ of a Cooper pair from $(\boldsymbol{k}'_F,-\boldsymbol{k}'_F)$ to $(\boldsymbol{k}'_F+\boldsymbol{Q},-\boldsymbol{k}'_F-\boldsymbol{Q})$ is dominated by the particle–hole fluctuation associated with the corresponding eigenvector at $\boldsymbol{Q}$. To clarify the degrees of freedom underlying this fluctuation, we further decompose the static particle–hole susceptibility $\hat{\chi}(\boldsymbol{q},0)$ into orbital-resolved spin and charge components. The

charge contribution is negligible compared to the spin channel and therefore not shown. The total spin susceptibility is defined as $\chi^{\rm S} = \sum_{\mu\nu}\chi^{\rm S}_{\mu\nu}(\boldsymbol{q})$, with orbital indices μ and ν. The individual component is given by

$$\chi^{\rm S}_{\mu\nu}(\boldsymbol{q}) = \int_0^\beta \frac{{\rm d}\tau}{N}\sum_{ll'}\langle T_\tau \boldsymbol{S}_{l\mu}(-\boldsymbol{q},\tau)\cdot\boldsymbol{S}_{l'\nu}(\boldsymbol{q},0)\rangle, \tag{3}$$

where l and l' denote sublattice indices. The spin susceptibilities of the $\mathrm{d}_{x^2\text{-}y^2}$-orbital and $\{\mathrm{d}_{xz},\mathrm{d}_{yz}\}$ orbitals are written as $\chi^{\rm S}_{\mathrm{d}_{x^2\text{-}y^2}} = \chi^{\rm S}_{\mathrm{d}_{x^2\text{-}y^2},\mathrm{d}_{x^2\text{-}y^2}}(\boldsymbol{q})$ and $\chi^{\rm S}_{\mathrm{d}_{xz}+\mathrm{d}_{yz}} = \sum_{\mu\nu\in\{\mathrm{d}_{xz},\mathrm{d}_{yz}\}}\chi^{\rm S}_{\mu\nu}(\boldsymbol{q})$, respectively. Similarly, the pairing kernel $\hat{M}^{\xi\xi'}_{n'n'}(\boldsymbol{k}_{\rm F},\boldsymbol{k}'_{\rm F})$ can be written as[40]

$$M^{\xi\xi'}(\boldsymbol{k}_{\rm F},\boldsymbol{k}'_{\rm F}) = \lambda_1 g_{{\rm R},\xi}(\boldsymbol{k}_{\rm F})g_{{\rm L},\xi'}(\boldsymbol{k}'_{\rm F}) + \cdots, \tag{4}$$

where $g_{{\rm R},\xi}(\boldsymbol{k}_{\rm F})$ and $g_{{\rm L},\xi'}(\boldsymbol{k}'_{\rm F})$ are the right and left eigenvectors of $M^{\xi\xi'}(\boldsymbol{k}_{\rm F},\boldsymbol{k}'_{\rm F})$, respectively. Symbol λ_1 denotes the largest eigenvalue of the pairing kernel. The ellipsis represents contributions from subleading eigenvalues. The singlet component of the pairing kernel projected onto the leading superconducting channel is given by $\lambda_1 g_{{\rm R},0}(\boldsymbol{k}_{\rm F})g_{{\rm L},0}(\boldsymbol{k}'_{\rm F})$. In the following calculations, since the triplet component of the pairing kernel is found to be negligible compared to the singlet component, we focus solely on the singlet channel. In this work, we employ a 100×100 $\boldsymbol{q}$-mesh and set the temperature to $k_{\rm B}T = 1/\beta = 0.001$ eV.

3. Results and discussion

Figure 2 exhibits the evolution of the leading instability channels as a function of the Hubbard interaction U and Hund's coupling $J_{\rm H}$. In Figs. 2(a) and 2(b), the left solid line marks the boundary separating the normal metal phase from the superconducting phase, determined by the condition that the leading eigenvalue λ of the gap equation (1) attains unity. The right solid line indicates the phase boundary between the superconducting and DW phases, determined by the Stoner criterion that the largest eigenvalue of $-\hat{V}\hat{\chi}_0(\boldsymbol{q},0)$ reaches unity. Within the normal metal phase where $\lambda < 1$, that is, the region to the left of the superconducting boundary, the dominant particle–particle instability is additionally presented. In the absence of SOC, the leading superconducting pairing initially favors A_{2g} symmetry for small U and $J_{\rm H}/U$. However, at larger values of $J_{\rm H}/U$, the leading pairing symmetry changes from A_{2g} to E_{2g} with the increase of U. With further enhancement of U, the system ultimately enters a SDW. When SOC is introduced, the leading superconducting pairing favors instead the E_{2g} symmetry, and at sufficiently large U, a particle–hole instability emerges as the dominant ordering tendency.

To elucidate the superconducting gap functions, we first analyze the case without SOC at two representative parameter sets: $J_{\rm H}/U = 0.2$, $U = 0.9964$ eV and $J_{\rm H}/U = 0.02$, $U = 1.0853$ eV [see Figs. 2(a) and 2(b)]. As illustrated in Fig. 2(c), these values of interaction parameters correspond to points where the leading eigenvalue λ of the linearized gap equation reaches unity. Figure 3(a) displays the gap function with A_{2g} symmetry, while Figs. 3(b) and 3(c) exhibit the two degenerate solutions with E_{2g} symmetry. The characteristic wave vectors $\boldsymbol{Q}_1 = (0.2252,-0.3900)$ and $\boldsymbol{Q}_2 = (0.4070,-0.2350)$, which connect regions with opposite signs of the gap function, coincide with the peak positions of the leading eigenvalues $\lambda^{\rm max}_\chi(\boldsymbol{q})$ of particle–hole susceptibility $\hat{\chi}(\boldsymbol{q},0)$ [Figs. 3(d) and 3(g)]. In the spin-fluctuation-mediated superconducting pairing scenario, the peak of eigenvalue $\lambda^{\rm max}_\chi(\boldsymbol{q})$ at wave vector $\boldsymbol{Q}$ $(=\boldsymbol{Q}_1,\boldsymbol{Q}_2)$ indicates that the pairing scattering is dominated by particle–hole fluctuation associated with the corresponding eigenvector at $\boldsymbol{Q}$, and that the pairing interaction satisfies $\Gamma^{00}(\boldsymbol{k}_{\rm F},\boldsymbol{k}'_{\rm F}) > 0$ where $\boldsymbol{k}_{\rm F} - \boldsymbol{k}'_{\rm F} = \boldsymbol{Q}$. To maximize the eigenvalue λ of the gap equation (1), the gap function must change sign between two FS points connected by these wave vectors (note the minus sign in Eq. (2)),[40,42,43] i.e., $\Delta_0(\boldsymbol{k}'_{\rm F}+\boldsymbol{Q})\Delta_0(\boldsymbol{k}'_{\rm F}) < 0$. For both sets of interaction parameters, the primary peaks for $\lambda^{\rm max}_\chi$ $(=\lambda^{\rm max}_\chi(\boldsymbol{q}))$ are located at $\boldsymbol{Q}_1$ and $\boldsymbol{Q}_2$, as shown in Figs. 3(e) and 3(h). These peaks are predominantly associated with spin fluctuations, as evidenced by the significant enhancement of the total spin susceptibility $\chi^{\rm S}$ [Figs. 3(e) and 3(h)]. The spin fluctuations at $\boldsymbol{Q}_1$ and $\boldsymbol{Q}_2$ originate primarily from the $\mathrm{d}_{x^2\text{-}y^2}$ orbital, as indicated by the pronounced peaks in $\chi^{\rm S}_{\mathrm{d}_{x^2\text{-}y^2}}$ [Figs. 3(e) and 3(h)]. These peaks are closely tied to the nesting of the β band,

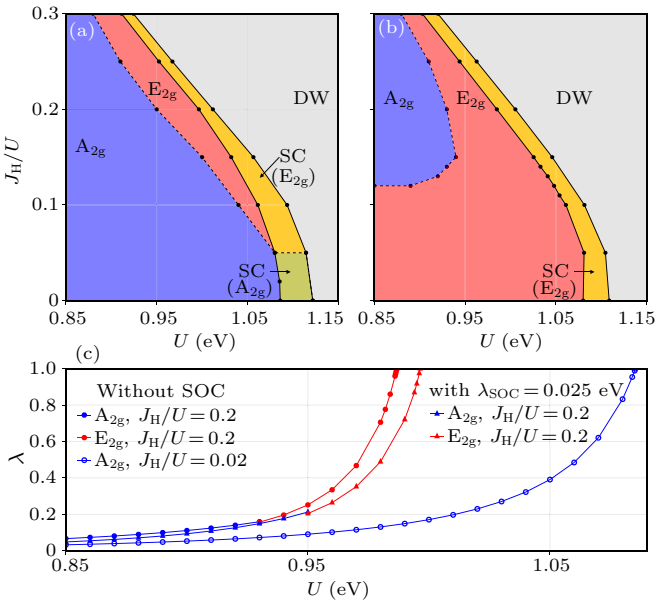

Fig. 2. Phase diagram depicting the leading instability channels within the RPA framework: (a) without SOC and (b) with SOC ($\lambda_{\rm SOC} = 0.025$ eV). The solid lines represent the phase boundaries, while the dashed lines indicate the crossover between the A_{2g} and E_{2g} pairing symmetry channels. SC and DW denote the superconducting and density-wave instabilities, respectively. (c) The leading eigenvalues λ of the linearized gap equations as a function of Hubbard interaction U.

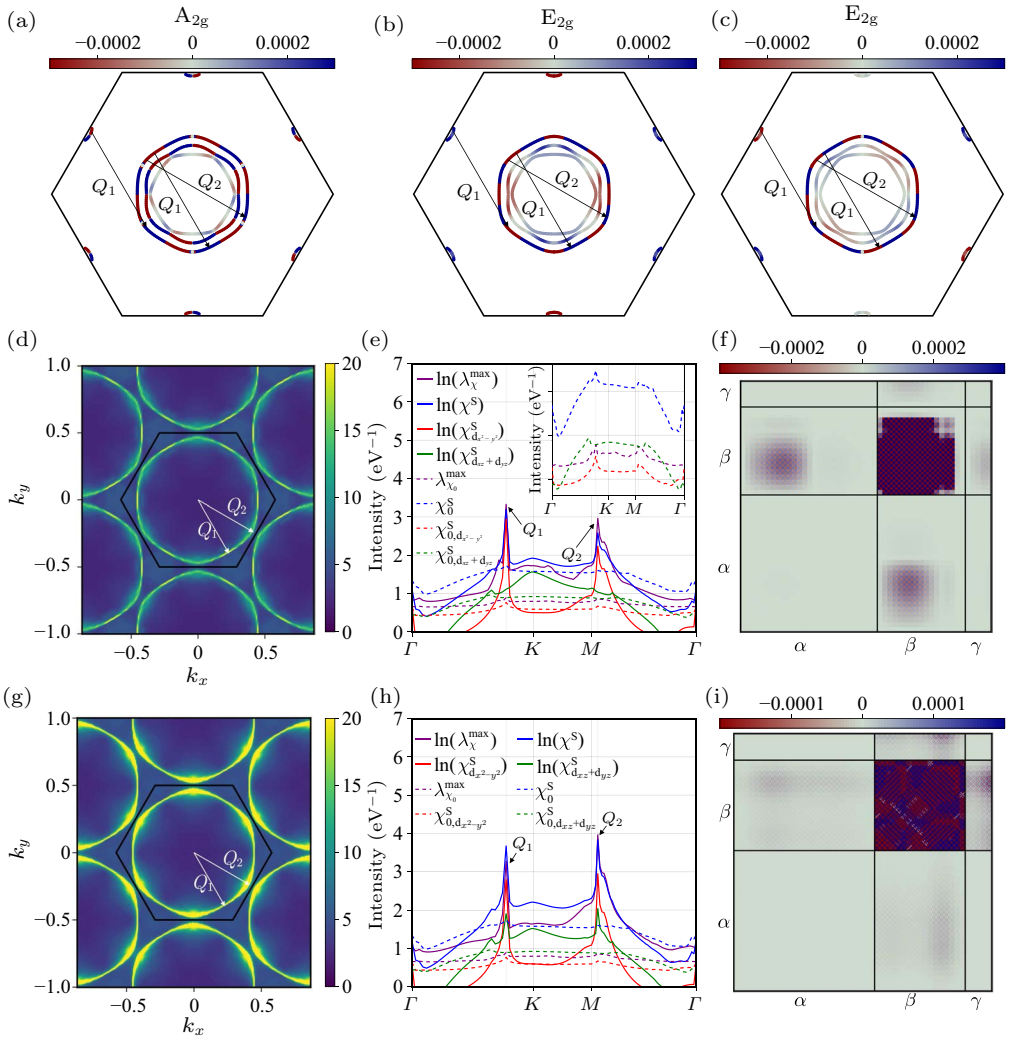

Fig. 3. (a) Superconducting gap function in the A_{2g} channel for $U = 1.0853$ eV, $J_H/U = 0.02$, and $\lambda_{SOC} = 0$ eV, corresponding to the largest eigenvalue $\lambda = 1.0$ of the linearized gap equations. (b), (c) Two degenerate gap functions in the E_{2g} channel for $U = 0.9964$ eV, $J_H/U = 0.2$, and $\lambda_{SOC} = 0$ eV, also with $\lambda = 1.0$. (d), (g) Maximum eigenvalues λ_χ^{max} of the particle–hole susceptibility $\hat{\chi}(\boldsymbol{q},0)$. The black line denotes the boundary of the first Brillouin zone, and the white arrows mark the wave vectors corresponding to susceptibility maxima. (e), (h) Static spin susceptibilities and eigenvalues λ_χ^{max}, $\lambda_{\chi_0}^{max}$. Both bare and dressed spin susceptibilities are scaled by $1/18$, with the dressed susceptibilities further shown on a logarithmic scale. Arrows highlight the positions of the prominent peaks. The inset in (e) shows a zoomed-in view of the bare susceptibilities. (f), (i) Singlet component of the pairing kernel for the A_{2g} and E_{2g} channels, respectively. The parameters sets $(J_H/U, U, \lambda_{SOC})$ used in (d), (e), (f) and (g), (h), (i) are the same as those in (a) and (b), (c), respectively.

which is mainly derived from the $d_{x^2-y^2}$ orbital [Fig. 1(c)]. The Fermi-surface-nesting origin of these peaks is further confirmed by examining the properties of the bare spin susceptibility $\chi^S_{0,d_{x^2-y^2}}$, whose characteristics are entirely determined by the FS, with no contribution from interaction effects. We find that $\chi^S_{0,d_{x^2-y^2}}$ exhibits clear maxima at $\boldsymbol{Q}_1$ and $\boldsymbol{Q}_2$ [inset of Fig. 3(e)], whereas $\chi^S_{0,d_{xz}+d_{yz}}$ lacks corresponding peaks. At small Hund's couplings, such as $J_H/U = 0.02$, the peak at $\boldsymbol{Q}_1$ exceeds that at $\boldsymbol{Q}_2$, stabilizing the A_{2g} pairing symmetry. In contrast, at larger Hund's couplings, such as $J_H/U = 0.2$, the $\boldsymbol{Q}_2$ peak becomes dominant, favoring the E_{2g} pairing symmetry. This evolution reflects the interplay between intra- and inter-orbital spin fluctuations. For weak Hund's coupling, the Hubbard interaction U enhances intra-orbital spin fluctuations, and the bare spin susceptibility in the dominant $d_{x^2-y^2}$-orbital channel exhibits a stronger peak at $\boldsymbol{Q}_1$ than that at $\boldsymbol{Q}_2$ [inset of Fig. 3(e)], leading to the dominance of $\boldsymbol{Q}_1$ in λ_χ^{max}. By contrast, at stronger Hund's coupling, the inter-orbital spin fluctuations are increased, as evidenced by the enhanced peaks for $\chi^S_{d_{xz}+d_{yz}}$ [Fig. 3(h)]. This shifts the leading peak to $\boldsymbol{Q}_2$. To shed light on the microscopic process behind the enhancement of inter-orbital spin fluctuations, we analyze the largest eigenvalue $\lambda_\chi^{max}(\boldsymbol{q})$ of $\hat{\chi}(\boldsymbol{q},0)$ together with its eigenvector $v_{l\nu}(\boldsymbol{q})$. The largest eigenvalue can be written as

$$\lambda_\chi^{max}(\boldsymbol{q}) = \frac{\sum_{ll'\nu\nu'} v^*_{l\nu}(\boldsymbol{q})[\hat{\chi}_0]^{l\nu}_{l'\nu'}(\boldsymbol{q},0)v_{l'\nu'}(\boldsymbol{q})}{1+D(\boldsymbol{q})}, \tag{5}$$

where $D(\boldsymbol{q}) = \sum_{ll'l_1\nu_1\mu\nu} v^*_{l\nu}(\boldsymbol{q})[\hat{V}]^{l\nu}_{l_1\nu_1}[\hat{\chi}_0]^{l_1\nu_1}_{l'\mu}(\boldsymbol{q},0)v_{l'\mu}(\boldsymbol{q})$. The corresponding particle–hole fluctuation mode is represented by the operator $\mathcal{O}(\boldsymbol{q}) = \sum_{l\nu} v_{l\nu}(\boldsymbol{q})S^z_{l\nu}(\boldsymbol{q})$, with the restriction to the S^z component enforced by spin-rotation symmetry without SOC. As shown in Fig. 5(a), the dominant weight of the eigenvector at $\boldsymbol{Q}_1$ originates from the $d_{x^2-y^2}$

orbital on both A and B sublattices (with $|v_{A,x^2\text{-}y^2}(\boldsymbol{q})|^2 = |v_{B,x^2\text{-}y^2}(\boldsymbol{q})|^2$), followed by subdominant contributions from the corresponding d_{xz} orbitals. At $\boldsymbol{Q}_2$, the weight is primarily from the B-sublattice $d_{x^2\text{-}y^2}$ orbital, with the next-largest and third-largest contributions from B-sublattice d_{xz} and d_{yz} orbitals, respectively. Accordingly, we restrict the summation in $D(\boldsymbol{q})$ to these dominant degrees of freedom. With increasing Hund's coupling, the weight shifts from the $d_{x^2\text{-}y^2}$ orbital to the d_{xz} and d_{yz} orbitals. Simultaneously, $-D(\boldsymbol{q})$ increases and approaches unity, with a notably faster increase at $\boldsymbol{Q}_2$ than at $\boldsymbol{Q}_1$ at large Hund's coupling, as shown in Fig. 5(a). This enhancement primarily stems from the contribution of the inter-orbital spin channel to $-D(\boldsymbol{q})$. These results demonstrate that Hund's coupling selectively enhances inter-orbital spin fluctuations, with a dominant effect at $\boldsymbol{Q}_2$, which consequently causes the leading peak in $\lambda_\chi^{\max}$ to shift from $\boldsymbol{Q}_1$ to $\boldsymbol{Q}_2$. In addition to the above analysis indicating that the pairing interaction originates primarily from the scattering channels within the β band, this conclusion is also supported by the singlet component of the pairing kernel. As demonstrated in Figs. 3(f) and 3(i), the pairing interaction within the β band is the strongest.

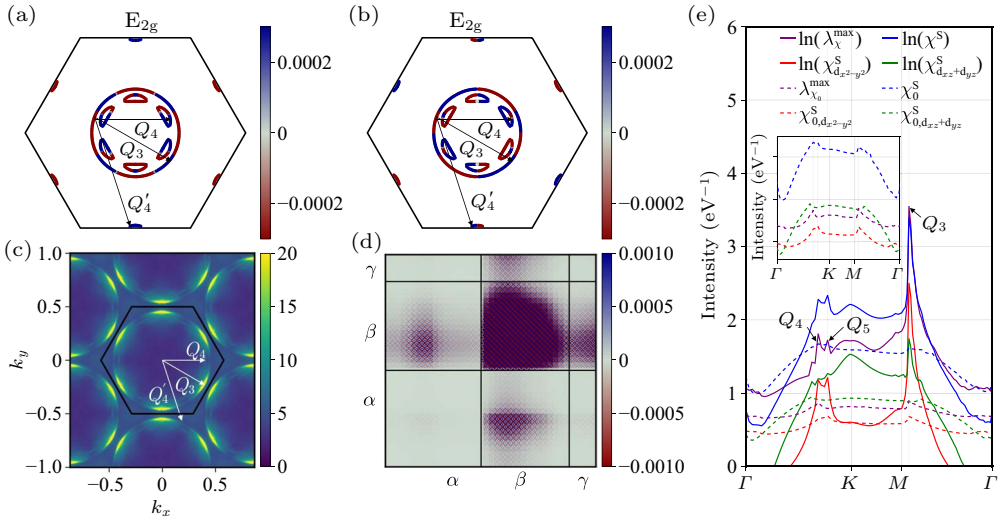

Fig. 4. (a), (b) Two degenerate gap functions in the E_{2g} channel. (c) Maximum eigenvalues of the particle–hole susceptibility $\hat{\chi}(\boldsymbol{q},0)$. The first Brillouin-zone boundary is outlined in black, and the dominant scattering vectors are indicated by white arrows. (d) Singlet component of the pairing kernel projected onto the leading E_{2g} channel. (e) Static spin susceptibilities plotted together with the leading eigenvalues $\lambda_\chi^{\max}$ ($\lambda_{\chi_0}^{\max}$). For this combined visualization, the bare spin susceptibilities are divided by 18, while the dressed spin susceptibilities are plotted as the logarithm of their values following the same scaling. Arrows mark the positions of the maxima. The inset shows a zoomed-in view of the bare susceptibilities. All results are for $U = 0.98675$ eV, $J_H/U = 0.2$, and $\lambda_{SOC} = 0.025$ eV, with largest eigenvalue $\lambda = 1.0$.

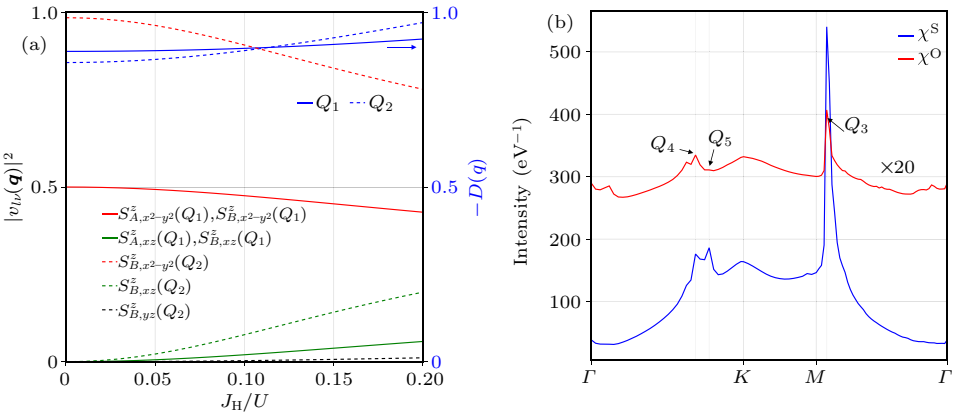

Fig. 5. Dominant components $|v_{l\nu}(\boldsymbol{q})|^2$ of the eigenvector corresponding to the largest eigenvalue $\lambda_\chi^{\max}$ of the particle–hole susceptibility $\hat{\chi}(\boldsymbol{q},0)$ at $\boldsymbol{Q}_1$ and $\boldsymbol{Q}_2$ as a function of J_H/U for $U = 0.9964$ eV in the absence of SOC. The blue solid (dashed) lines denotes $-D(\boldsymbol{q})$ (see main text) at $\boldsymbol{Q}_1$ ($\boldsymbol{Q}_2$), plotted against the right-hand y-axis as indicated by the blue arrow. (b) Dressed orbital (χ^O) and spin (χ^S) susceptibility for $U = 0.98675$ eV, $J_H/U = 0.2$, and $\lambda_{SOC} = 0.025$ eV. The dressed orbital susceptibility χ^O is scaled by a factor of 20 for visual comparison.

Next, we discuss the cases with SOC. Since the results for $\lambda_{SOC} = 25$–40 meV[44] are qualitatively similar, owing to the unchanged Fermi-surface topology, we present the results only for the case of $\lambda_{SOC} = 25$ meV in Fig. 4. When SOC is included, the leading superconducting instability favors E_{2g} symmetry. The two degenerate gap functions in this channel are illustrated in Figs. 4(a) and 4(b) for $J_H/U = 0.2$ and $U = 0.98675$ eV. The characteristic wave vectors $\boldsymbol{Q}_3 = (0.3984, -0.2300)$, $\boldsymbol{Q}_4 = (0.3984, 0.000)$, and $\boldsymbol{Q}_4' = (0.1867, -0.5748)$, linking Fermi-surface regions with

opposite signs of the gap function, align with the maxima of $\lambda_\chi^{\max}$ [Fig. 4(c)]. Among these vectors, the leading and subleading peaks in $\lambda_\chi^{\max}$ occur at $\boldsymbol{Q}_3$ and $\boldsymbol{Q}_4$, respectively [Fig. 4(e)]. At $\boldsymbol{Q}_3$, the dominant peak of $\lambda_\chi^{\max}$ is predominantly driven by spin fluctuations, consistent with the significant enhancement of the total spin susceptibility χ^{S} at this wave vector. The subleading peak at $\boldsymbol{Q}_4$ reflects an increased contribution from orbital fluctuations. This is evident from the fact that although the peak of χ^{S} at $\boldsymbol{Q}_5 = (0.4503, 0.0000)$ is larger than that at $\boldsymbol{Q}_4$, the situation is reversed in $\lambda_\chi^{\max}$, suggesting an additional orbital contribution at $\boldsymbol{Q}_4$. To further confirm the presence of additional orbital fluctuations, we compute the orbital susceptibility χ^{O}, defined as $\chi^{\mathrm{O}} = \sum_{ll's_1s_2}\sum_{\mu\nu\mu'\nu'}[\hat{\chi}]^{l\mu s_1,l\nu s_1}_{l'\nu's_2,l'\mu's_2}(\boldsymbol{q},0)O_{\nu\mu}O_{\nu'\mu'}$ (see Appendix B). As shown in Fig. 5(b), the dressed orbital susceptibility χ^{O} exhibits a pronounced peak at $\boldsymbol{Q}_4$, in contrast to its intensity at $\boldsymbol{Q}_5$, verifying the existence of additional orbital fluctuations. Consistent with the case without SOC, the dominant pairing interaction remains within the β band, as confirmed by the singlet component of the pairing kernel [Fig. 4(d)]. However, compared to the scenario without SOC, the inter-band pairing interaction between the β and α bands is enhanced, aligning with the above analysis that additional orbital fluctuations at $\boldsymbol{Q}_4$ play a role with increasing SOC. The interband pairing interaction between the β and γ bands is also enhanced, as shown in Fig. 4(d). One representative channel is the $\boldsymbol{Q}_4'$-mediated scattering, where $\boldsymbol{Q}_4'$ connects the β and γ bands [Fig. 4(a)], as illustrated in Fig. 4(c).

4. Summary

In summary, we have theoretically investigated the superconducting pairing symmetry in pressurized $CsCr_3Sb_5$ using an effective four-orbital tight-binding model combined with RPA analysis. Our results reveal that the strong Hund's coupling enhances the inter-orbital spin fluctuations, and results in a shift in the maximum of spin fluctuations from the Γ–K direction to the Γ–M direction. The significantly enhanced inter-orbital spin fluctuations promote a superconducting gap function with E_{2g} symmetry. In the case of a small Hund's coupling, where the inter-orbital spin fluctuations are weak, the leading pairing symmetry is A_{2g} symmetry. The inclusion of SOC enhances the orbital fluctuations and stabilizes the E_{2g} symmetry. In both scenarios with and without SOC, the β band, which is mainly derived from the $d_{x^2-y^2}$ orbital, provides the prominent contribution to the pairing interaction.

Appendix A: First-principles calculations and tight-binding model

The first-principles calculations were performed using Vienna *ab initio* simulation package (VASP)[45] with the projector augmented-wave method.[46] The exchange–correlation interactions were modeled using the Perdew–Burke–Ernzerhof (PBE) form of the generalized gradient approximation (GGA).[47] A Γ-centered k-point grid of dimensions $12\times12\times5$ was implemented in the self-consistent calculations. To avoid double counting of the SOC, the SOC was not included in these calculations.

Guided by symmetry analysis under the D_{6h} point Group assumption, we derive an effective tight-binding model, which can be represented as a 10×10 matrix[34]

$$H_{\mathrm{t}} = \sum_{\boldsymbol{k},\sigma}\hat{\Psi}^\dagger_\sigma(\boldsymbol{k})\begin{pmatrix}\hat{T}_{AA} & \hat{T}_{AB} & \hat{T}^\dagger_{CA} & \hat{T}_{Ap}\\ \hat{T}^\dagger_{AB} & \hat{T}_{BB} & \hat{T}_{BC} & \hat{T}_{Bp}\\ \hat{T}_{CA} & \hat{T}^\dagger_{BC} & \hat{T}_{CC} & \hat{T}_{Cp}\\ \hat{T}^\dagger_{Ap} & \hat{T}^\dagger_{Bp} & \hat{T}^\dagger_{Cp} & T_{pp}\end{pmatrix}\hat{\Psi}_\sigma(\boldsymbol{k}), \tag{A1}$$

where A, B, and C denote the sublattice indices. The fermionic operator $\hat{\Psi}_\sigma(\boldsymbol{k})$ is defined as

$$\hat{\Psi}^\dagger_\sigma(\boldsymbol{k}) = \left[d^{\dagger A}_{xz,\sigma}(\boldsymbol{k}), d^{\dagger A}_{yz,\sigma}(\boldsymbol{k}), d^{\dagger A}_{x^2-y^2,\sigma}(\boldsymbol{k}), d^{\dagger B}_{xz,\sigma}(\boldsymbol{k}), d^{\dagger B}_{yz,\sigma}(\boldsymbol{k}), d^{\dagger B}_{x^2-y^2,\sigma}(\boldsymbol{k}), d^{\dagger C}_{xz,\sigma}(\boldsymbol{k}), d^{\dagger C}_{yz,\sigma}(\boldsymbol{k}), d^{\dagger C}_{x^2-y^2,\sigma}(\boldsymbol{k}), p^\dagger_{z,\sigma}(\boldsymbol{k})\right], \tag{A2}$$

where the subscript σ indicates the spin indices. The orbital indices are xz, yz, x^2-y^2 for the Cr-d orbitals and p_z for the Sb_1-p_z orbital. The hopping matrices $\hat{T}_{AA}$, $\hat{T}_{AB}$, $\hat{T}_{Ap}$, and $\hat{T}_{pp}$ are given by[34]

$$\hat{T}_{AA} = \begin{bmatrix}t_3 & 0 & 0\\ 0 & t_4 & 0\\ 0 & 0 & t_3'\end{bmatrix}2\cos(k_1) + \begin{bmatrix}t_5 & t_6 & 0\\ t_6 & t_7 & 0\\ 0 & 0 & t_3''\end{bmatrix}2\cos(k_3) + \begin{bmatrix}t_5 & -t_6 & 0\\ -t_6 & t_7 & 0\\ 0 & 0 & t_3''\end{bmatrix}2\cos(k_2) + \begin{bmatrix}\mu_{xz} & 0 & 0\\ 0 & \mu_{yz} & 0\\ 0 & 0 & \mu_{x^2-y^2}\end{bmatrix},$$

$$\hat{T}_{AB} = 2\begin{bmatrix}t_{xx} & t_{xy} & 0\\ -t_{xy} & t_{yy} & 0\\ 0 & 0 & t_1'\end{bmatrix}\cos\left(\frac{k_3}{2}\right) + 2\begin{bmatrix}t_{xx}' & t_{xy}' & 0\\ -t_{xy}' & t_{yy}' & 0\\ 0 & 0 & t_2'\end{bmatrix}\cos\left(k_1+\frac{k_3}{2}\right) + \begin{bmatrix}0 & 0 & 0\\ 0 & 0 & 0\\ 0 & 0 & 2t_4'\left(\cos\left(k_2+\frac{k_3}{2}\right)+\cos\left(k_1-\frac{k_3}{2}\right)\right)+2t_5'\cos\left(\frac{3k_3}{2}\right)\end{bmatrix},$$

$$\hat{T}_{Ap} = \begin{bmatrix} t_{pxz} 2\mathrm{i}\sin\left(\frac{k_2+k_3}{2}\right) \\ t_{pyz} 2\mathrm{i}\sin\left(\frac{k_1}{2}\right) \end{bmatrix},$$
$$T_{pp} = 2t_p(\cos(k_1)+\cos(k_2)+\cos(k_3))+\mu_p + 2t_{pp}(\cos(k_3-k_1)+\cos(k_2+k_1) + \cos(k_3+k_2)), \quad \text{(A3)}$$

where $k_1 = \boldsymbol{k}\cdot\boldsymbol{a_1}$, $k_2 = \boldsymbol{k}\cdot\boldsymbol{a_2}$, and $k_3 = \boldsymbol{k}\cdot(\boldsymbol{a_2}-\boldsymbol{a_1})$. $\boldsymbol{a}_1$ and $\boldsymbol{a}_2$ are the lattice vectors. The hopping matrices $\hat{T}_{BB}$ ($\hat{T}_{Bp}$) and $\hat{T}_{CC}$ ($\hat{T}_{Cp}$) can be obtained by changing the parameters (k_1,k_2,k_3) in $\hat{T}_{AA}$ ($\hat{T}_{Ap}$) to $(-k_2,-k_3,k_1)$ and $(k_3,-k_1,-k_2)$, respectively. The explicit hopping parameters were determined through a least-squares optimization procedure that minimizes the deviation between the DFT-calculated bands and those derived from the effective tight-binding model. The hopping parameters for $CsCr_3Sb_5$ at 5 GPa are listed in Table 1.

Table A1. Hopping parameters and their values, expressed in units of eV.

Parameter	Value	Parameter	Value	Parameter	Value
t_{xx}	–0.259	t_{xy}	–0.207	t_{yy}	0.395
t'_{xx}	–0.148	t'_{xy}	0.162	t'_{yy}	0.073
t_3	–0.021	t_4	0.071	t_5	–0.053
t_6	0.062	t_7	–0.132	t'_1	–0.408
t'_2	0.006	t'_3	–0.056	t''_3	–0.021
t'_4	–0.008	t'_5	0.025	μ_{xz}	–0.285
μ_{yz}	–1.336	$\mu_{x^2\text{-}y^2}$	-0.514	t_p	–0.133
μ_p	0.575	t_{pyz}	0.068	t_{pp}	–0.019
t_{pxz}	0.055				

In the chosen orbital basis d_{xz}, d_{yz}, and $d_{x^2\text{-}y^2}$, the orbital angular momentum operator l_i of the Cr ions can be expressed in matrix form as

$$l_x = \begin{bmatrix} 0 & 0 & 0 \\ 0 & 0 & \mathrm{i} \\ 0 & -\mathrm{i} & 0 \end{bmatrix}, \quad l_y = \begin{bmatrix} 0 & 0 & \mathrm{i} \\ 0 & 0 & 0 \\ -\mathrm{i} & 0 & 0 \end{bmatrix}, \quad l_z = \begin{bmatrix} 0 & -\mathrm{i} & 0 \\ \mathrm{i} & 0 & 0 \\ 0 & 0 & 0 \end{bmatrix}. \quad \text{(A4)}$$

Appendix B: The details of RPA

The bare particle–hole susceptibility $\hat{\chi}_0$ is defined as

$$[\hat{\chi}_0]^{\alpha_1\alpha_2}_{\alpha_3\alpha_4}(\boldsymbol{q},\mathrm{i}\omega_n) = \frac{1}{N}\int_0^\beta \mathrm{d}\tau\, \mathrm{e}^{\mathrm{i}\omega_n\tau}\sum_{\boldsymbol{k}\boldsymbol{k}'}\langle T_\tau c^\dagger_{\boldsymbol{k}\alpha_2}(\tau)c_{\boldsymbol{k}-\boldsymbol{q}\alpha_1}(\tau)c^\dagger_{\boldsymbol{k}'-\boldsymbol{q}\alpha_3}(0)c_{\boldsymbol{k}'\alpha_4}(0)\rangle_0, \quad \text{(B1)}$$

where ω_n represents a fermionic Matsubara frequency and T_τ denotes the time-ordering operator with respect to the imaginary time. The average $\langle\cdots\rangle_0$ depends on $\mathrm{e}^{-\beta H_0}$ with inverse temperature $\beta = 1/k_\mathrm{B}T$. H_0 is the quadratic part of the Hamiltonian H. The subscript $\alpha_n = (l_n,\mu_n,\sigma_n)$ denotes the sublattice l_n, orbital μ_n, and spin σ_n indices. The Fourier-transformed fermionic operators are written as

$$c^\dagger_{\boldsymbol{k}\alpha} = \frac{1}{\sqrt{N}}\sum_i c^\dagger_{i\alpha}\mathrm{e}^{\mathrm{i}\boldsymbol{k}\cdot(\boldsymbol{r}_i+\boldsymbol{\delta}_l)}, \quad c_{\boldsymbol{k}\alpha} = \frac{1}{\sqrt{N}}\sum_i c_{i\alpha}\mathrm{e}^{-\mathrm{i}\boldsymbol{k}\cdot(\boldsymbol{r}_i+\boldsymbol{\delta}_l)}, \quad \text{(B2)}$$

where $\boldsymbol{r}_i$ denotes the lattice vector corresponding to the ith unit cell and $\boldsymbol{\delta}_l$ represents an intra-unitcell vector with sublattice l. In the normal state, the bare particle–hole susceptibility $\hat{\chi}_0$ becomes

$$[\hat{\chi}_0]^{\alpha_1\alpha_2}_{\alpha_3\alpha_4}(\boldsymbol{q},\mathrm{i}\omega_n) = -\frac{1}{N}\sum_{\boldsymbol{k}n_1n_2}[u^{\alpha_2}_{n_1}(\boldsymbol{k})]^* u^{\alpha_4}_{n_1}(\boldsymbol{k})\frac{f(\varepsilon_{\boldsymbol{k},n_1})-f(\varepsilon_{\boldsymbol{k}-\boldsymbol{q},n_2})}{\mathrm{i}\omega_n+\varepsilon_{\boldsymbol{k},n_1}-\varepsilon_{\boldsymbol{k}-\boldsymbol{q},n_2}}[u^{\alpha_3}_{n_2}(\boldsymbol{k}-\boldsymbol{q})]^* u^{\alpha_1}_{n_2}(\boldsymbol{k}-\boldsymbol{q}), \quad \text{(B4)}$$

where $u^\alpha_n(\boldsymbol{k}) = \langle\alpha|\boldsymbol{k}n\rangle$ is the projection of eigenvector onto α state, corresponding to the eigenvalue $\varepsilon_{\boldsymbol{k},n}$ of H_0. The function $f(\varepsilon_{\boldsymbol{k},n_1})$ represents the Fermi distribution function. Within the RPA framework, the particle–hole susceptibility $\hat{\chi}$ is given by

$$\hat{\chi}(\boldsymbol{q},\mathrm{i}\omega_n) = \hat{\chi}_0(\boldsymbol{q},\mathrm{i}\omega_n)[1+\hat{V}(\boldsymbol{q})\hat{\chi}_0(\boldsymbol{q},\mathrm{i}\omega_n)]^{-1}, \quad \text{(B4)}$$

where $\hat{V}(\boldsymbol{q})$ is the bare particle–hole vertex. For the multi-orbital Hubbard-type interaction, defined as

$$H_\mathrm{I} = U\sum_{i,l\mu}\hat{n}_{il\mu\uparrow}\hat{n}_{il\mu\downarrow} + \left(U'-\frac{J_\mathrm{H}}{2}\right)\sum_{il,\mu<\nu,\sigma\sigma'}\hat{n}_{il\mu\sigma}\hat{n}_{il\nu\sigma'} - 2J_\mathrm{H}\sum_{il,\mu<\nu}\boldsymbol{S}_{il\mu}\cdot\boldsymbol{S}_{il\nu} + J_\mathrm{P}\sum_{il,\mu\neq\nu}c^\dagger_{il\mu\uparrow}c^\dagger_{il\mu\downarrow}c_{il\nu\downarrow}c_{il\nu\uparrow}, \quad \text{(B5)}$$

the bare particle–hole vertex $\hat{V}(\boldsymbol{q})$ satisfies

$$H_\mathrm{I} = \frac{1}{2N}\sum_{\boldsymbol{k}\boldsymbol{k}'\boldsymbol{q}\alpha_1\alpha_2\alpha_3\alpha_4}[\hat{V}(\boldsymbol{q})]^{\alpha_1\alpha_2}_{\alpha_3\alpha_4}c^\dagger_{\boldsymbol{k}-\boldsymbol{q}\alpha_1}c_{\boldsymbol{k}\alpha_2}c^\dagger_{\boldsymbol{k}'\alpha_4}c_{\boldsymbol{k}'-\boldsymbol{q}\alpha_3}, \quad \text{(B6)}$$

where, in this instance, the $\boldsymbol{q}$-independent interaction vertex $\hat{V}(\boldsymbol{q})$ can be expressed as a combination of spin ($\hat{U}_\mathrm{s}$) and charge ($\hat{U}_\mathrm{c}$) vertices,

$$[\hat{V}]^{l_1\mu_1\sigma_1,l_2\mu_2\sigma_2}_{l_3\mu_3\sigma_3,l_4\mu_4\sigma_4} = \frac{1}{2}\delta_{l_1l_2}\delta_{l_3l_4}\delta_{l_1l_3}([\hat{U}_\mathrm{c}]^{\mu_1\mu_2}_{\mu_3\mu_4}\delta_{\sigma_1\sigma_2}\delta_{\sigma_3\sigma_4} - [\hat{U}_\mathrm{s}]^{\mu_1\mu_2}_{\mu_3\mu_4}\boldsymbol{\sigma}_{\sigma_1\sigma_2}\cdot\boldsymbol{\sigma}^*_{\sigma_3\sigma_4}). \quad \text{(B7)}$$

The non-zero elements of the charge and spin vertices are re-

spectively given by[40,42,43]

$$[\hat{U}_{\rm c}]^{\mu\mu}_{\mu\mu} = U, \quad [\hat{U}_{\rm c}]^{\mu\nu}_{\mu\nu} = 2J_{\rm H} - U',$$
$$[\hat{U}_{\rm c}]^{\mu\mu}_{\nu\nu} = 2U' - J_{\rm H}, \quad [\hat{U}_{\rm c}]^{\mu\nu}_{\nu\mu} = J_{\rm P}, \ \text{with} \ \mu \neq \nu, \tag{B8}$$
$$[\hat{U}_{\rm s}]^{\mu\mu}_{\mu\mu} = U, \quad [\hat{U}_{\rm s}]^{\mu\nu}_{\mu\nu} = U',$$
$$[\hat{U}_{\rm s}]^{\mu\mu}_{\nu\nu} = J_{\rm H}, \quad [\hat{U}_{\rm s}]^{\mu\nu}_{\nu\mu} = J_{\rm P}, \ \text{with} \ \mu \neq \nu. \tag{B9}$$

In this work, we adopt the relationships $U' = U - 2J_{\rm H}$ and $J_{\rm P} = J_{\rm H}$.

The spin or charge susceptibilities could be obtained from the generalized particle–hole susceptibility $\hat{\chi}(\boldsymbol{q}, {\rm i}\omega_n)$ by projecting onto the spin or charge channels. Specifically, the total spin susceptibility is given by

$$[\hat{\chi}]^{ab}(\boldsymbol{q}, {\rm i}\omega_n) = \int_0^\beta \frac{{\rm d}\tau}{N} {\rm e}^{{\rm i}\omega_n\tau} \sum_{ll'\mu\nu} \langle T_\tau S^a_{l\mu}(-\boldsymbol{q},\tau) S^b_{l'\nu}(\boldsymbol{q},0)\rangle$$
$$= \sum_{ll'\mu\nu} \sum_{s_1 s_2 s_3 s_4} \sigma^a_{s_2 s_1} [\hat{\chi}]^{l\mu s_1, l\mu s_2}_{l'\nu s_3, l'\nu s_4}(\boldsymbol{q}, {\rm i}\omega_n) \sigma^b_{s_3 s_4}, \tag{B10}$$

where $\sigma^{a=x,y,z}$ represents the Pauli matrix. To obtain the other physical susceptibilities, such as orbital susceptibility, similar projections can be performed. For instance, the orbital susceptibility $\chi^{\rm O}$ discussed in the main text is defined as

$$\chi^{\rm O} = \int_0^\beta \frac{{\rm d}\tau}{N} \langle T_\tau \mathfrak{O}(-\boldsymbol{q},\tau) \mathfrak{O}(\boldsymbol{q},0)\rangle$$
$$= \sum_{ll' s_1 s_2} \sum_{\mu\nu\mu'\nu'} [\hat{\chi}]^{l\mu s_1, l\nu s_1}_{l'\nu' s_2, l'\mu' s_2}(\boldsymbol{q},0) O_{\nu\mu} O_{\nu'\mu'}, \tag{B11}$$

where the orbital matrix O is expressed in the basis of d_{xz}, d_{yz}, and $d_{x^2\text{-}y^2}$ orbitals as

$$O = \begin{bmatrix} 0 & 0 & -{\rm i} \\ 0 & 0 & -{\rm i} \\ {\rm i} & {\rm i} & 0 \end{bmatrix}. \tag{B12}$$

To examine the possible particle–hole instabilities, we consider the static susceptibility $\hat{\chi}(\boldsymbol{q},0)$. The instability occurs when $\det(1+\hat{V}\hat{\chi}_0(\boldsymbol{q},0)) = 0$. Equivalently the emergence of a particle–hole instability is indicated when the largest eigenvalue of the matrix $-\hat{V}\hat{\chi}_0(\boldsymbol{q},0)$ reaches unity. The computation is restricted to the submatrix of $-\hat{V}\hat{\chi}_0(\boldsymbol{q},0)$ defined by the set of indices $(\alpha_1\alpha_2, \alpha_3\alpha_4)$, where $[\hat{V}]^{\alpha_1\alpha_2}_{\alpha_3\alpha_4} \neq 0$, since these terms provide the dominant contributes near the critical point. A similar restriction is applied in evaluating the largest eigenvalue $\lambda^{\rm max}_\chi$ of the particle–hole susceptibility $\hat{\chi}(\boldsymbol{q},0)$.

For the analysis of superconductivity, we focus on the pairing function with zero center momentum. The effective pairing interaction by spin-fluctuations within RPA can be written as[40,41]

$$[\hat{\Gamma}(\boldsymbol{k},\boldsymbol{k}')]^{\alpha_1\alpha_2}_{\alpha_3\alpha_4} = [\hat{V}]^{\alpha_1\alpha_3}_{\alpha_4\alpha_2} - [\hat{V}\hat{\chi}(\boldsymbol{k}-\boldsymbol{k}',0)\hat{V}]^{\alpha_1\alpha_3}_{\alpha_4\alpha_2}$$
$$+ [\hat{V}\hat{\chi}(\boldsymbol{k}+\boldsymbol{k}',0)\hat{V}]^{\alpha_1\alpha_4}_{\alpha_3\alpha_2}. \tag{B13}$$

Due to the prevalence of scattering events occurring in proximity to the FS, attention is directed towards the pairing interactions among the states located on the FS. The effective pairing interaction on the FS is given by

$$\Gamma^{\xi\xi'}(\boldsymbol{k}_{\rm F}, \boldsymbol{k}'_{\rm F}) = \sum_{\varsigma_1\varsigma_2\varsigma_3\varsigma_4} \sum_{\alpha_1\alpha_2\alpha_3\alpha_4} u^{*\alpha_1}_{n_1\varsigma_1}(\boldsymbol{k}_{\rm F}) \hat{\gamma}^{\dagger\xi}_{\varsigma_1\varsigma_2} u^{*\alpha_2}_{n_1\varsigma_2}(-\boldsymbol{k}_{\rm F}) [\hat{\Gamma}(\boldsymbol{k}_{\rm F}, \boldsymbol{k}'_{\rm F})]^{\alpha_1\alpha_2}_{\alpha_3\alpha_4} u^{\alpha_3}_{n_2\varsigma_3}(\boldsymbol{k}'_{\rm F}) \hat{\gamma}^{\xi'}_{\varsigma_3\varsigma_4} u^{\alpha_4}_{n_2\varsigma_4}(-\boldsymbol{k}'_{\rm F}), \tag{B14}$$

where subscript n_1 and ς_1 denote the band and pseudo-spin space, respectively. If the band indices n_1 or n_2 do not correspond to a band at the Fermi surface, the Fermi-surface projected pairing interaction $\Gamma^{\xi\xi'}(\boldsymbol{k}_{\rm F}, \boldsymbol{k}'_{\rm F})$ necessarily vanishes. Therefore, the band indices need not be explicitly written in the pairing interaction $\Gamma^{\xi\xi'}(\boldsymbol{k}_{\rm F}, \boldsymbol{k}'_{\rm F})$. The $\hat{\gamma}^\xi$ matrices are defined as

$$\hat{\gamma}^\xi = \frac{1}{\sqrt{2}} \sigma^\xi {\rm i}\sigma^y. \tag{B15}$$

Here, $\sigma^{\xi=0}$ represents the 2×2 identity matrix . The symbol $\hat{\gamma}^0$ signifies the pseudo-spin singlet, whereas $\hat{\gamma}^\xi$ denotes the pseudo-spin triplet, with ξ belonging to the set $\{x,y,z\}$. Owing to the gauge freedom inherent in the eigenstate resolution process, we implement the symmetry-adapted methodology outlined in Ref. [40] to circumvent non-unique gauge selections.

In order to categorize the pairing functions, the projection operator is utilized to map these functions onto the irreducible representation space associated with the corresponding point group. The projection operator is given by

$$P^i_\mu = \frac{l_i}{g} \sum_{R\in G} D^i(R)^*_{\mu\mu} P_R, \tag{B16}$$

where $D^i(R)$ is the i-th irreducible representation of point group G with an order of g. The notation P_R denotes the symmetry operator corresponding to the element R in the symmetry group G. l_i denotes the dimension of the i-th irreducible representation space. The crystal structure of $CsCr_3Sb_5$ possesses D_{6h} point group symmetry, which comprises twelve irreducible representations: A_{1g}, A_{2g}, B_{1g}, B_{2g}, E_{1g}, E_{2g}, A_{1u}, A_{2u}, B_{1u}, B_{2u}, E_{1u}, and E_{2u}.

Acknowledgements

This work was supported by the National Key Research and Development of China (Grant Nos. 2024YFA1408104

and 2021YFA1400400), the National Natural Science Foundation of China (Grant Nos. 12374137, 12434005, 12074175, 92165205, 12004191, and 12550405), and the Natural Science Foundation of Jiangsu Province (Grant No. BK20233001).

References

[1] Balents L 2010 *Nature* **464** 199
[2] Norman M R 2016 *Rev. Mod. Phys.* **88** 041002
[3] Wen J, Rüegg A, Wang C C J and Fiete G A 2010 *Phys. Rev. B* **82** 075125
[4] Tang E, Mei J W and Wen X G 2011 *Phys. Rev. Lett.* **106** 236802
[5] Yu S L and Li J X 2012 *Phys. Rev. B* **85** 144402
[6] Kiesel M L and Thomale R 2012 *Phys. Rev. B* **86** 121105
[7] Wang W S, Li Z Z, Xiang Y Y and Wang Q H 2013 *Phys. Rev. B* **87** 115135
[8] Kiesel M L, Platt C and Thomale R 2013 *Phys. Rev. Lett.* **110** 126405
[9] Kang M, Ye L, Fang S, You J S, Levitan A, Han M, Facio J I, Jozwiak C, Bostwick A, Rotenberg E, Chan M K, McDonald R D, Graf D, Kaznatcheev K, Vescovo E, Bell D C, Kaxiras E, van den Brink J, Richter M, Prasad Ghimire M, Checkelsky J G and Comin R 2020 *Nat. Mater.* **19** 163
[10] Wu Y M, Thomale R and Raghu S 2023 *Phys. Rev. B* **108** L081117
[11] Chen H, Hu B, Ye Y, Yang H and Gao H J 2022 *Chin. Phys. B* **31** 97405
[12] Neupert T, Denner M M, Yin J X, Thomale R and Hasan M Z 2022 *Nat. Phys.* **18** 137
[13] Yin J X, Lian B and Hasan M Z 2022 *Nature* **612** 647
[14] Wang Y, Wu H, McCandless G T, Chan J Y and Ali M N 2023 *Nat. Rev. Phys.* **5** 635
[15] Jiang K, Wu T, Yin J X, Wang Z, Hasan M Z, Wilson S D, Chen X and Hu J 2023 *Natl. Sci. Rev.* **10** nwac199
[16] Wilson S D and Ortiz B R 2024 *Nat. Rev. Mater.* **9** 420
[17] Yu F H, Wu T, Wang Z Y, Lei B, Zhuo W Z, Ying J J and Chen X H 2021 *Phys. Rev. B* **104** L041103
[18] Jiang Y X, Yin J X, Denner M M, Shumiya N, Ortiz B R, Xu G, Guguchia Z, He J, Hossain M S, Liu X, Ruff J, Kautzsch L, Zhang S S, Chang G, Belopolski I, Zhang Q, Cochran T A, Multer D, Litskevich M, Cheng Z J, Yang X P, Wang Z, Thomale R, Neupert T, Wilson S D and Hasan M Z 2021 *Nat. Mater.* **20** 1353
[19] Chen H, Yang H, Hu B, Zhao Z, Yuan J, Xing Y, Qian G, Huang Z, Li G, Ye Y, Ma S, Ni S, Zhang H, Yin Q, Gong C, Tu Z, Lei H, Tan H, Zhou S, Shen C, Dong X, Yan B, Wang Z and Gao H J 2021 *Nature* **599** 222
[20] Grandi F, Consiglio A, Sentef M A, Thomale R and Kennes D M 2023 *Phys. Rev. B* **107** 155131
[21] Ortiz B R, Teicher S M L, Hu Y, Zuo J L, Sarte P M, Schueller E C, Abeykoon A M M, Krogstad M J, Rosenkranz S, Osborn R, Seshadri R, Balents L, He J and Wilson S D 2020 *Phys. Rev. Lett.* **125** 247002
[22] Yin Q, Tu Z, Gong C, Fu Y, Yan S and Lei H 2021 *Chin. Phys. Lett.* **38** 37403
[23] Ortiz B R, Sarte P M, Kenney E M, Graf M J, Teicher S M L, Seshadri R and Wilson S D 2021 *Phys. Rev. Mater.* **5** 034801
[24] Feng X, Jiang K, Wang Z and Hu J 2021 *Sci. Bull.* **66** 1384
[25] Liu Y, Liu Z Y, Bao J K, Yang P T, Ji L W, Wu S Q, Shen Q X, Luo J, Yang J, Liu J Y, Xu C C, Yang W Z, Chai W L, Lu J Y, Liu C C, Wang B S, Jiang H, Tao Q, Ren Z, Xu X F, Cao C, Xu Z A, Zhou R, Cheng J G and Cao G H 2024 *Nature* **632** 1032
[26] Liu L, Li Y, Tan H, Liu Y, Shi Y, Zhai Y, Lin H, Cao G, Yan B, Zhang G M and Yang L 2024 arXiv:2411.06778 [cond-mat.str-el]
[27] Yao W, Liu S, Xu Z, Ishikawa D, Wang Z, Gao B, Xu S, Ye F, Hashimoto K, Shibauchi T, Baron A Q R and Dai P 2024 arXiv:2410.16465 [cond-mat.str-el]
[28] Wang Z, Guo Y, Huang H Y, Xie F, Huang Y, Gao B, Oh J S, Wu H, Okamoto J, Channagowdra G, Chen C T, Ye F, Lu X, Liu Z, Ren Z, Fang Y, Wang Y, Biswas A, Zhang Y, Yue Z, Hu C, Jozwiak C, Bostwick A, Rotenberg E, Hashimoto M, Lu D, Kono J, Chu J H, Yakobson B I, Birgeneau R J, Cao G H, Fujimori A, Huang D J, Si Q, Yi M and Dai P 2025 *Nat. Commun.* **16** 7573
[29] Li Y, Liu Y, Du X, Wu S, Zhao W, Zhai K, Hu Y, Zhang S, Chen H, Liu J, Yang Y, Peng C, Hashimoto M, Lu D, Liu Z, Wang Y, Chen Y, Cao G and Yang L 2025 *Nat. Commun.* **16** 3229
[30] Peng S, Han Y, Li Y, Shen J, Miao Y, Luo Y, Huai L, Ou Z, Li H, Xiang Z, Liu Z, Shen D, Hashimoto M, Lu D, Yao Y, Qiao Z, Wang Z and He J 2024 arXiv:2406.17769 [cond-mat.supr-con]
[31] Wang Y 2025 *Phys. Rev. B* **111** 035127
[32] Xie F, Fang Y, Li Y, Huang Y, Chen L, Setty C, Sur S, Yakobson B, Valentí R and Si Q 2025 *Phys. Rev. Res.* **7** L022061
[33] Xu C, Wu S, Zhi G X, Cao G, Dai J, Cao C, Wang X and Lin H Q 2025 *Nat. Commun.* **16** 3114
[34] Wang W, Yu S L and Li J X 2025 *Phys. Rev. B* **112** 165137
[35] Wu S, Xu C, Wang X, Lin H Q, Cao C and Cao G H 2025 *Nat. Commun.* **16** 1375
[36] Wu X, Schwemmer T, Müller T, Consiglio A, Sangiovanni G, Di Sante D, Iqbal Y, Hanke W, Schnyder A P, Denner M M, Fischer M H, Neupert T and Thomale R 2021 *Phys. Rev. Lett.* **127** 177001
[37] Vafek O and Chubukov A V 2017 *Phys. Rev. Lett.* **118** 087003
[38] Saito T, Yamakawa Y, Onari S and Kontani H 2015 *Phys. Rev. B* **92** 134522
[39] Liu L, Okazaki K, Yoshida T, Suzuki H, Horio M, Ambolode L C C, Xu J, Ideta S, Hashimoto M, Lu D H, Shen Z X, Ota Y, Shin S, Nakajima M, Ishida S, Kihou K, Lee C H, Iyo A, Eisaki H, Mikami T, Kakeshita T, Yamakawa Y, Kontani H, Uchida S and Fujimori A 2017 *Phys. Rev. B* **95** 104504
[40] Scherer D D and Andersen B M 2019 arXiv:1909.01313
[41] Rømer A T, Scherer D D, Eremin I M, Hirschfeld P J and Andersen B M 2019 *Phys. Rev. Lett.* **123** 247001
[42] Yu S L and Li J X 2013 *Chin. Phys. B* **22** 87411
[43] Yao Z J, Li J X and Wang Z D 2009 *New J. Phys.* **11** 25009
[44] Grinberg M, Lesniewski T, Mahlik S and Liu R S 2017 *Opt. Mater.* **74** 93
[45] Kresse G and Hafner J 1993 *Phys. Rev. B* **47** 558
[46] Blöchl P E 1994 *Phys. Rev. B* **50** 17953
[47] Perdew J P, Burke K and Ernzerhof M 1997 *Phys. Rev. Lett.* **78** 1396